# Design, Construction, and Characterization of a Magic Angle Field Spinning RF Magnet

Javier Alonso-Valdesueiro, Beatriz Sisniega, Irati Rodrigo, Jorge Pérez-Muñoz, Juan-Mari Collantes, and Fernando Plazaola

***Abstract*— Magic angle field spinning (MAFS) is a Nuclear Magnetic Resonance (NMR) spectroscopy technique used in NMR Compact Devices to enhance the spectral resolution. In this technique, the sample is placed inside a magnet which generates a magnetic flux density oriented at 54.74° with respect to the sample main axis and spun at high frequencies. We present here, the design and construction of a novel magnet that generates a magnetic field according to the MAFS technique. The prototype generates two radio frequency and one dc magnetic fields by the combined action of three electromagnets. This combination results in a magnetic flux density of ∼10 mT, with field deviations ≤1% inside a cylindrical volume of 30 × 30 mm, an orientation easily controlled by field amplitudes and precessing at frequencies up to 12 kHz. The magnet has been characterized by using a novel Flux+Gauss meter (FGM) built and calibrated *in-house*. The FGM is able to measure ac and dc magnetic fields along seven different longitudinal axes, one of them corresponds to the longitudinal axis of the prototype. The other six axes are placed at six angular orientations on a 30-mm-diameter circumference. The characterization of the magnet includes field profiles of the RF and dc fields along the FGM axes and deviations of the field in the 30 × 30 mm cylinder. The homogeneity is evaluated as the relative differences between the field measured at the centered axis and the field measured along the six extra axes for both RF and dc fields.**

***Index Terms*— Instrumentation and measurement, magnetic field measurement, magnetic resonance imaging (MRI), nuclear magnetic resonance (NMR), radio frequency.**

## I. Introduction

MAGIC angle field spinning (MAFS) is a technique presented in the 1960s to the Nuclear Magnetic Resonance (NMR) community [1] and tested at Berkeley in the 2000s [2], [3]. The technique skews the main internuclear interaction (dipolar–dipolar coupling [4]) responsible for reducing the spectral resolution in NMR experiments with solid samples [5]. This skewing process is achieved by placing the solid sample inside a magnetic field oriented at 54.74° with respect to the longitudinal axis of the experimental device and rotating the field at a certain spinning frequency, $\Omega_{ROT}$. When the NMR experiment of a solid sample takes place under these circumstances [6], it results in a dramatically narrowed spectrum compared with the spectrum obtained in regular NMR experiments.

The fact that the sample remains static with respect to the magnetic field presents a considerable advantage compared with another magic angle spinning (MAS) techniques [7], [8]. Typically, in MAS NMR experiments, the sample is oriented at 54.74° with respect to a strong magnetic field and spun at kilohertz frequencies. Therefore, in order to reduce the solid interactions and sample anisotropies, MAFS technique is the perfect candidate to increase image resolution in Magnetic Resonance Imaging (MRI) [9] where the patient cannot be spun at kilohertz frequencies as the sample is in MAS NMR experiments [10], [11].

In this direction, there is an increasing interest in producing a MAFS magnetic field for MRI experiments. Some designs include a superconducting magnet spinning at low frequencies [12], [13] where the cryogenic fluids are also spun and replaced during experiments. Some other groups have developed assemblies of permanent magnets producing a tilted magnetic field and they have spun mechanically the magnet achieving spinning frequencies up to 10 Hz [14], [15].

This approach presents two inconveniences. First, the spinning frequency of the magnetic field is not high enough. It is found that line narrowing in NMR MAS experiments is appreciable when $\Omega_{ROT} \gg \langle \Delta\omega \rangle$ holds, where $\langle \Delta\omega \rangle$ is the square root of the absorption line of the sample in a static field [1]. Therefore, when spinning frequencies are limited to 10 Hz, many of the interactions that decrease the resolution in MRI images are not canceled.

Second, the final prototypes consist of heavy magnets (300–500 kg) attached to voluminous instruments for mechanical spinning and massive electronic instrumentation. Considering the electronics needed during the MRI experiment, these solutions would need a room for safe functionality. Moreover, safety rules in medical environments make the applicability of these solutions barely possible.

In this paper, we present the design, construction, and characterization of a novel electromagnet for NMR–MRI experiments with application in mobile environments such as emergency rooms and medical ambulances. The prototype overcomes the two disadvantages of the MAFS magnets presented earlier. It produces a magnetic flux density, $B_{MAFS}$,

Manuscript received July 10, 2018; revised October 25, 2018; accepted November 11, 2018. Date of publication December 21, 2018; date of current version September 13, 2019. This work was supported in part by the Marie Sklodowska-Curie through the European Union's Horizon 2020 Research and Innovation Program under Grant 750445 and in part by the Culture, Linguistics, Politics and Education Department, Basque Country Government under Grant IT1104-16. *(Corresponding author: Javier Alonso-Valdesueiro.)*

J. Alonso-Valdesueiro, B. Sisniega, J. Pérez-Muñoz, J.-M. Collantes, and F. Plazaola are with the Faculty of Science and Technology, University of the Basque Country, 48940 Leioa, Spain (e-mail: javier.alonsov@ehu.eus).

I. Rodrigo is with BCMaterials, Basque Center for Materials, Applications and Nanostructures, University of the Basque Country, 48940 Leioa, Spain.

Color versions of one or more of the figures in this article are available online at http://ieeexplore.ieee.org.

Digital Object Identifier 10.1109/TIM.2018.2884606

of $\sim$1.5 mT/$A_{rms}$ ($A_{rms}$ is the root-mean-square value of the current flowing through the coil), with deviations of the intensity $\leq$1% in a cylindrical volume of 30 $\times$ 30 mm (height $\times$ diameter) and spinning frequencies up to 12 kHz. The magnetic field can be oriented at 54.74° with respect to the sample by controlling the amplitude ratio of a rotating and a static magnetic field. These fields are both generated inside the magnet by the assembly of three concentric coils working together. The rotating magnetic field is produced by two transverse resonators on the transverse plane of the assembly (*xy* plane). The static field is oriented along the longitudinal axis of the device ($z$-axis) and created by a double Helmholtz pair surrounding the transverse resonators. Our aim is to present a proof of concept of the technology behind the production of the RF-MAFS field. Therefore, the homogeneity of the different components of the field, a key parameter in NRM and MRI experiments, is evaluated in accordance with other designs where the homogeneity limit is $\sim$5000 part per million (ppm) [16]–[20].

Most commercial Fluxmeters and Gaussmeters measuring ac or dc magnetic fields at frequencies higher than 3 kHz and intensities higher than 500 $\mu$T are expensive, and their dimensions do not fit in the design of our prototype. At the same time, the most accurate way of measuring magnetic fields, an NMR spectrometer [21], is not available in our laboratory. Therefore, in order to characterize the RF and dc fields, we have designed and built a Flux+Gauss meter (FGM) able to measure ac and dc fields in the required range of frequencies and intensities ($\Omega \geq$ 3 kHz and $B \geq$ 500 $\mu$T). We present the information about the FGM and the control platform which allow us to characterize the magnetic flux densities inside our prototype along different longitudinal axes. We also present information about the calibration method [22] that ensures the correct measurements of the MAFS field.

This paper is then organized as follows. First, in Section II, the MAFS concept is described with detail. We describe the different coils forming the assembly, their design, and final configuration. In Section III, the *in-house* built magnetic FGM is addressed. We present information about the calibration process and the measurement capabilities. The characterization of the magnet is detailed in Section IV and, finally in Section V, we summarize this paper and the performance of the MAFS RF magnet.

## II. MAFS Electromagnet

The MAFS electromagnet generates a magnetic flux density, $B_{MAFS}$, precessing at $\theta_{MAFS}$ with respect to its longitudinal axis, $z$-axis. Fig. 1(a) shows the arrangement of the different magnetic flux densities involved in the production of $B_{MAFS}$. Its precession is provided by a rotating magnetic flux density, $B_{ROT}$, with a rotating frequency $\Omega_{ROT}$. This $B_{ROT}$ can be generated by the combination of two linearly polarized magnetic flux densities, $B_{1,2}$, spatially oriented as depicted in Fig. 1(b). They both oscillate at the same frequency, $\Omega_1 = \Omega_2 = \Omega_{ROT}$ but 90° out of phase. The orientation of $B_{MAFS}$ is controlled by the intensity ratio $B_{ROT}/B_z = \tan(\theta_{MAFS})$.

Our prototype is depicted in Fig. 2. The magnetic assembly consists of two transverse resonators, $Tr_{1,2}$, producing $B_1$ and

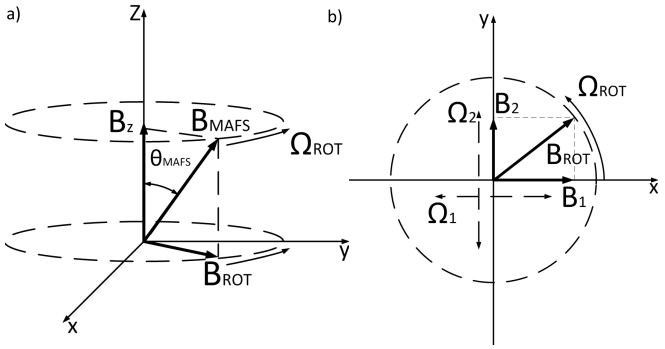


Fig. 1. Magnetic flux densities of the MAFS field. (a) Processing magnetic field consists of two components. The precession is provided by a rotating magnetic flux density, $B_{ROT}$ spinning in the plane perpendicular to the longitudinal axis of the device. The tilting angle is controlled by the intensity ratio of $B_{ROT}$ and $B_z$. (b) $B_{ROT}$ can be created by two linearly polarized magnetic flux densities, oriented at 90° with respect to each other and oscillating 90° out of phase. The frequencies of $B_{1,2}$, $\Omega_{1,2}$, respectively, define $\Omega_{ROT}$ of $B_{ROT}$.

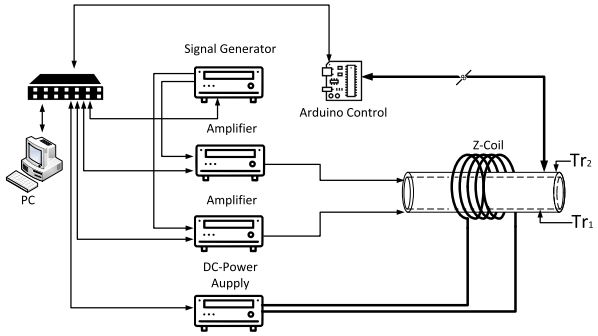


Fig. 2. Design of the MAFS prototype. The RF signals are generated with 90° phase shift with respect to each other. They are amplified by two power amplifiers attached to $Tr_{1,2}$. A dc-power supply feeds the $Z$-coil. The magnetic assembly ($Tr_{1,2}$ and $Z$-coil) is controlled in temperature by an ARDUINO-based platform and a PC. The system is monitored by a PC through Ethernet connection.

$B_2$ and a double Helmholtz pair coil ($Z$-coil) producing $B_z$. Two sinusoidal signals with frequencies up to 12 kHz and 90° out of phase with respect to each other are provided by the signal generator. They are separately amplified and transferred to $Tr_{1,2}$.

The system is controlled by a PC connected through Ethernet to the different devices. In order to prevent any damage of the magnetic assembly, the temperature is monitored during experiments. Resistive temperature sensors are placed in different points and the temperature data is acquired by an ARDUINO-based platform.

### A. Transverse Resonators $Tr_{1,2}$

There are different transverse resonators that could produce $B_{1,2}$ [23] (see Fig. 1). However, most of them are designed with small inner bores and dimensions. Therefore, a different design is needed in our case. The double helix dipole (DHD) coil [24], has been used in particle accelerators for many years to generate the transverse magnetic fields for particle guiding. Its design offers high amplitude and large homogeneous volume of transverse magnetic flux densities.

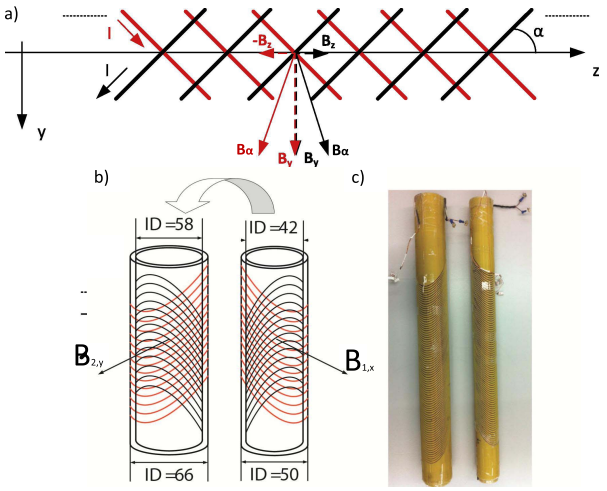


Fig. 3. Conceptual description of the DHD coil. (a) Combination of two tilted coil fed by currents flowing in opposite direction produces $2B_y$. (b) Two concentric double layered FR4 tubes with IDs = 42, 50, 58, 66 mm carved with 2 mm grooves where a 1.9-mm single strand wire is placed. The winding corresponds to an helical coil tilted an angle $\alpha = 30°$ and winding pitch d = 5 mm. (c) Practical realization of $Tr_{1,2}$. Power cabling and the temperature sensors can be observed in the photography already in place.

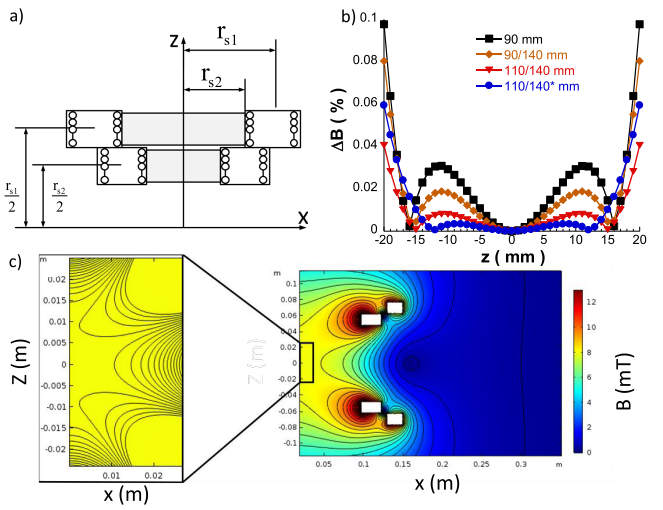


Fig. 4. Homogeneity along the $z$-axis for the configurations presented in Table I. (a) Schematic of the double Helmholtz pair where the distance between each ring has been set to the radius, $r_s$. (b) ▼-configuration shows a homogeneity lower than 0.01%. However, this configuration results in a practical winding of 270 m of wire. Therefore, a configuration with two layers less than the previous one was also tested in order to reduce the amount of wire (●). It results in a deviation of ∼0.01% along the $z$-axis. (c) Contour plot of the homogeneity in the $zx$ plane obtained from simulations for the ● configuration taken every 20 $\mu$T. The contour levels in the zoomed-in view area are taken every 1 $\mu$T.

We have constructed two of these resonators, $Tr_{1,2}$, and assembled them concentrically [see Fig. 3(b)]. In order to achieve a cylindrical volume of the homogeneous magnetic field of 30 × 30 mm, the minimum inner bore diameter of the resonators must be ∼42 mm. This diameter allows us to easily accommodate the sample and the future coils needed for NMR/MRI experiments like MRI Gradient and RF transceiver coil. Therefore, $Tr_1$ consists of two 3-mm-thick concentric FR4 tubes with an inner diameter (ID) = 42 mm and ID = 50 mm. They act as holders of the first DHD coil wound with 1.9-mm single strain wire. In the same way, $Tr_2$ consists of other two 3-mm-thick concentric FR4 tubes with ID = 58 mm and ID = 66 mm holding the second DHD coil wound with the same wire. The tubes were carved with 2-mm-deep square grooves forming a helical winding tilted an angle $\alpha = 30°$ and a winding pitch, $d$, of 5 mm. This configuration produces maximum amplitude of the magnetic fields generated at the center of both resonators while $\alpha$ and $d$ ensure the mechanical feasibility of both structures. A final description of these resonators working together is depicted in Fig. 3(b) and their practical realization is shown in Fig. 3(c). This practical realization was carried out by a company which manufactured the necessary tools and carved the profiles on material based on epoxy resin. Once the four cylinders were received in-house, the coils were wound and glued with an epoxy resin that holds the wire in place. The cylinders were placed concentrically and held tight by glue tape which allowed their free movement in order to perform the manual alignment mentioned above.

With this configuration, numerical integration of Biot–Savart law predict magnetic flux densities of ∼1.5 and ∼1.3 $mT/A_{rms}$ for $B_{1,2}$, respectively. Each resonator shows an orthogonal component ($B_2$ for $Tr_1$ and $B_1$ for $Tr_2$) ≤1% inside a cylindrical volume of 30 × 30 mm. Measurements presented in Section IV validate the numerical simulations allowing us to predict magnetic flux densities of future designs.

### B. Double Helmholtz Pair, Z-Coil

$B_z$ is the static component of $B_{MAFS}$. Therefore, in comparison with the linear components of $B_{ROT}$, $B_{1,2}$, its inhomogeneities are not averaged by any rotation. Consequently, the design of the coil producing $B_z$ was focused on obtaining very small intensity deviations, $\Delta B_z$ inside a cylinder of 30 × 30 mm.

We have performed simulations of different configurations of the $Z$-coil with COMSOL multiphysics. An optimization process was performed on multiple Helmholtz pairs working together with some constraints on power and dimensions. First, the total power dissipated by the $Z$-coil was constrained to 200 W which is the maximum power we can dissipate without including complicate cooling systems. Second, the maximum radius of the Helmholtz pairs was constrained to 150 mm and the distance to the center of each pair to 200 mm. These dimensions fit well in the aluminum frame where the electromagnet was installed (see Section II-C). Third, the amount of cable available in the laboratory for the practical winding of the coil was limited to 200 m. Table I shows the possible configurations for one and two Helmholtz pairs [see Fig. 4(a)]. Fig. 4(b) shows the homogeneity along the longitudinal axis of the coils when it is calculated with the following equation for the configurations of Table I:

$$\Delta B_z(\%) = \frac{|B_0 - B(z)|}{B_0} \times 100 \tag{1}$$

where $B_0$ is the magnetic flux density at $z = 0$ and $B_{(z)}$ is the magnetic flux density along the $z$-axis [see Fig. 4(a)]. The optimization process had a goal of 8 mT at the center of the

TABLE I
DIFFERENT RADII, POSITIONS, AND CURRENTS FOR ONE AND TWO HELMHOLTZ COILS PRODUCING $B_z$

| $N_{Helm} = 1$ | | | | $N_{Helm} = 2$ | | | |
|---|---|---|---|---|---|---|---|
| **Radii (mm)** | **$N_{turns}$** | **Current (A)** | **Power (W)** | **Radii (mm)** | **$N_{turns}$** | **Current (A)** | **Power (W)** |
| 80 | 200 | 3.56 | 24.12 | $r_1 = 90$<br>$r_2 = 140$ | $N_1 = 105$<br>$N_2 = 84$ | 5.04 | $P_1 = 17.74$<br>$P_2 = 22.08$ |
| 90 | 200 | 4.02 | 34.32 | $r_1 = 110$<br>$r_2 = 140$ | $N_1 = 105$<br>$N_2 = 84$ | 5.73 | $P_1 = 27.98$<br>$P_2 = 28$ |

$Z$-coil. The best compromise between homogeneity and power dissipation is achieved with the ▼-configuration. However, the amount of copper wire of this configuration (∼270 m) was too high to consider its practical realization. Therefore, the ●-configuration with two layers less per pair than ▼-configuration was constructed. This configuration consists of ∼198 m of 1.9-mm single-strand copper wire wound around the structure depicted in Fig. 4(a). Each layer is held together with epoxy resin and the total resistance of the $Z$-coil is ∼3 Ω.

Fig. 4(c) shows the detail of a contour plot of the homogeneity in the $xz$ plane obtained from simulations. The contour levels were taken every 1 $\mu$T. As we expected, changes along 30 mm of the $z$-axis were around 0.01%. In the radial direction, we observed deviations around 0.07%. Therefore, the expected homogeneity is around 0.07% inside the cylindrical volume of 30 × 30 mm around the center of the coil.

### C. Final Assembly

Fig. 5 shows the design and realization of the novel RF-MAFS magnet. The assembly is ∼1.1 m tall and ∼15 kg weight. $Tr_{1,2}$ are placed one inside the other and oriented manually. The two pairs of the $Z$-coil are placed at 70 and 55 mm, respectively, from the center of the assembly. These three electromagnets are enclosed in an aluminum frame grounded in order to avoid parasite radiation inside the coils and reduce the electromagnetic (EM) radiation outside. On top of the aluminum frame, an insertion and connection port allows us to attach the FGM and rotate it around the $z$-axis in six different positions. This port also includes electrical connections for $Tr_{1,2}$ and the $Z$-coil.

The current amplifiers, AR3501AH (see Fig. 2), are connected to $Tr_{1,2}$ through low inductance twisted wire and programed by the PC to provide up to 13 $A_{rms}$ each in a frequency range up to 12 kHz. The phase of the input signals (coming from an AFG3102 signal generator) is also controlled by the PC in order to compensate the misalignment of $Tr_{1,2}$. A KIKUSUI bipolar power supply is connected to the $Z$-coil providing up to ±10 A over a 4 Ω-load in a controlled way. We have not included any noise mitigation method for the current source.

## III. FLUX AND GAUSS METER DESIGN AND TEST

### A. Description of the System

In order to characterize the magnetic assembly presented earlier, an integrated FGM was designed, built, and calibrated

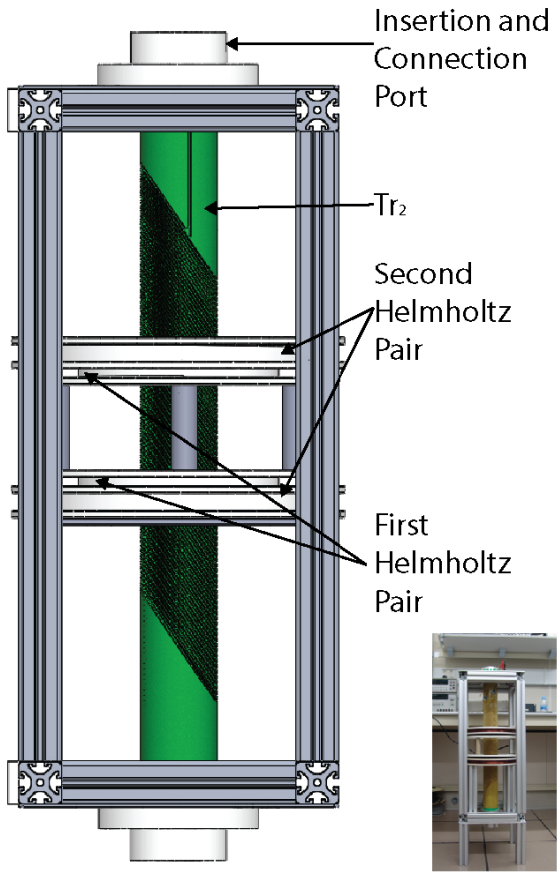


Fig. 5. Prototype of the novel RF-MAFS magnet placed in our laboratory. The Aluminum frame is grounded in order to avoid parasite radiation inside the magnet. The final assembly (down right corner) is a portable device of 1.1 m height and 15 kg weight with connection ports for $Tr_{1,2}$, the $Z$-coil and the FGM. Note that in the design $Tr_1$ is inside $Tr_2$.

in-house. It consists of a mobile platform pushed up and down by a stepper motor that is controlled by an ARDUINO-based device. A PC controls the movement of the motor in steps ≥2 mm. Fig. 6 shows the conceptual scheme of the system and its practical realization. We have minimized the amount of metallic parts in the mobile platform in order to avoid any undesired perturbation of the $B_{ROT}$ field. Therefore, all the parts were 3-D-printed or based on epoxy resin.

The RF sensors depicted in Fig. 6(b) consist of two pairs of pick-up coils separated 15 mm to each other. Each pair has two 2 × 2 $mm^2$, four turns, squared coils orientated in quadrature as depicted in Fig. 7, allowing us the detection of two perpendicular components of the magnetic field in the

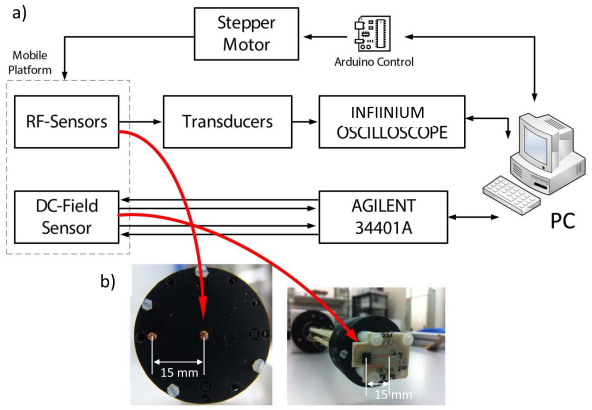


Fig. 6. Measurement system of $B_{\mathrm{MAFS}}$. (a) Mobile platform is controlled by and ARDUINO-based device and the measurement is organized by the PC. The PC orders the ARDUINO to move the platform, and once is moved, it triggers the measurement in the oscilloscope. At the end, $V_{pp}$ is read and processed by the PC and a new measurement starts. The mobile platform is attached to the motor through a polylactic acid and fiberglass structure. At the end of the structure, a printed circuit board (PCB) allows connection of the different sensors. (b) Pick-up coil sensing $B_{\mathrm{ROT}}$ and Hall sensors measuring $B_z$. Both sets of pick-up coils are placed on the same plane 15 mm away from each other. The Hall sensors are placed one on top of the other (3 mm apart) and 15 mm away from each other.

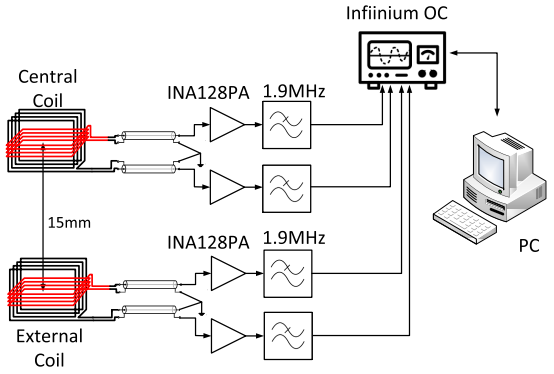


Fig. 7. Details of the measurement chain for $B_{\mathrm{ROT}}$. The pick-up coils are wound around the square structure which is a $2 \times 2$ mm$^2$ section. The windings are four turns of 0.25-mm copper wire and they are connected to the ending PCB by a coaxial cable from LAKESHORE. The induced voltage is amplified by two instrumentation amplifiers and their output measured by an oscilloscope. The measurement chain results in a voltage resolution of $\pm 0.5$ mV which theoretically corresponds to $\sim \pm 26$ $\mu$T.

$xy$ plane. Each set is connected to two INA128PA instrumentation amplifiers by a coaxial cable from LAKESHORE. After low-pass filtering, their output goes to an INFINIUM A-series oscilloscope where the RF signals oscillating at the two orientations are measured. After 5 mm displacement of the platform, the PC triggers the measurement in the oscilloscope. It takes 16 scans and averages the input signal before the PC reads the value of the peak-to-peak voltage. The measurement chain is depicted in Fig. 7, and it results in a voltage resolution of $\pm 0.5$ mV which theoretically corresponds to $\sim \pm 26$ $\mu$T.

The dc-Field sensors are two AD22151 Hall sensors, placed 15 mm away to each other and configured to provide $V_{\mathrm{cc}}/2 + 11.56$ mV/G $\times B_z$ and $V_{\mathrm{cc}}/2 + 40.85$ mV/G $\times B_z$ at the center and 15 mm away, respectively. The supply voltages and the output signals were routed outside the RF-MAFS magnet through an eight-wire twisted cable. The output voltage was measured with an AGILENT 34401A multimeter controlled by the PC. The input current was measured by recording the voltage on a noninductive 10-$\Omega$ resistor. In the same way, we measure the RF magnetic field, the PC takes 16 values of the voltage measured with the Agilent multimeter and averages the final result. In this way, the resolution is defined by the maximum rms noise of the Hall sensors for the selected gains. We observed $\sim \pm 20$ and $\sim \pm 70$ $\mu$T at the center and 15 mm away respectively.

### B. Calibration

A calibration experiment was performed in order to obtain the transfer function of the pick-up coils and the Hall sensors and determine the accuracy of our FGM. In the calibration of both type of sensors (RF and dc), we used available commercial devices.

For the Hall sensors, a commercial longitudinal Gaussmeter was placed at the center of the $Z$-coil and 15 mm away in the same plane when 1 A was flowing through the coil. The measurement was recorded ($1225 \pm 10$ and $1228 \pm 10$ $\mu$T, respectively) and then the same measurement was performed with the Hall sensors placed in the mobile platform [see Fig. 6(b)]. Correction factors of $+28$ and $-25$ $\mu$T where obtained for both Hall sensors (centered and 15 mm away from the center).

In this calibration process, a temperature drift of 0.5 $\mu$T/s of $B_z$ was observed. This drift is related to the heating process of the $Z$-coil observed in every resistive magnet without refrigeration. Besides the simple refrigeration techniques that can be implemented in order to mitigate this drift, an electronic control of the output current of the power supply feeding the $Z$-coil must be developed. The KIKUSUI power supply provides a control system of its output current of 1 mA every 0.1 s with which, in the case of long experiments (more than 30 s in this case), the temperature drift of the magnetic field at the center of the magnet could be compensated by a control program working at the PC.

For the pick-up coils, a commercial three-axis Fluxmeter (Mag585 from Bartington, Inc.) was placed at the geometrical center of the concentric DHD coils. $\mathrm{Tr}_2$ was oriented properly with respect to the measurement axis of the Fluxmeter and fed with 1 $\mathrm{A}_{\mathrm{rms}}$ at 1 kHz. First, measurements of the magnetic flux density were performed with the Fluxmeter oriented in six different directions between 0° and 180°. Second, the measurement tip was placed in the same geometrical position than the Fluxmeter and the measurements were taken at the same six angular orientations. The same procedure was performed for the pick-up coils placed 15 mm away from the center of the tip. Fig. 8(a) and (b) shows the absolute errors for both sets of pick-up coils. These errors were used to correct the measurement that characterizes $B_{\mathrm{ROT}}$.

It is important to note that the commercial instruments used during the calibration allowed us to perform measurements in particular locations inside the final assembly. However, they were not suitable for performing a complete characterization of the three electromagnets due to their dimensions and their limited measurement capabilities.

TABLE II
SOURCES OF UNCERTAINTY IDENTIFIED DURING THE DESIGN AND TEST OF THE FGM

| $\mathbf{B}_{1,2}$ **Meas.** | | | $\mathbf{B}_z$ **Meas.** | | | |
|---|---|---|---|---|---|---|
| **Source** | **Deviation** | **% Error** | **Source** | Sensor | **Deviation** | **% Error** |
| $\theta_\Delta$ | 0.0013 | $\pm 0.13$ | $\theta_\Delta$ | $\mathrm{HS}_{cent}$<br>$\mathrm{HS}_{15\,mm}$ | $3.8 \times 10^{-5}$<br>$3.8 \times 10^{-5}$ | $\pm 0.004$<br>$\pm 0.004$ |
| $\Delta G_v$ | 0.00094 | $\pm 0.09$ | $\Delta G_v$ | $\mathrm{HS}_{cent}$<br>$\mathrm{HS}_{15\,mm}$ | $0.156\,^{mV}/_{mT}$<br>$0.156\,^{mV}/_{mT}$ | $\pm 0.15$<br>$\pm 0.4$ |
| $\Delta I_{Tr}$ | $3.5\,\mathrm{mA}_{rms}$ | $\pm 0.35$ | $\Delta I_{Hel.}$ | $\mathrm{HS}_{cent}$<br>$\mathrm{HS}_{15\,mm}$ | $7.15\,\mu\mathrm{T}$<br>$7.15\,\mu\mathrm{T}$ | $\pm 0.5$<br>$\pm 0.5$ |

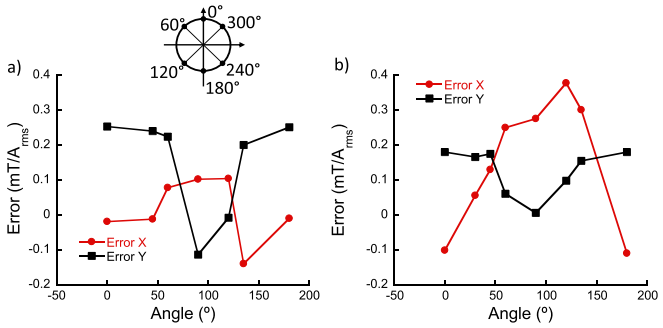


Fig. 8. Calibration curves of the FGM for the pick-up coils. (a) Absolute errors of the central pick-up coils with respect to the measurements performed with the mag585 Fluxmeter in six different angular orientations. (b) Absolute errors of the pick-up coils placed 15 mm away from the center of the measurement tip with respect to the measurements performed with the mag585 Fluxmeter in seven different angular orientations.

### C. Sources of Uncertainty in Homogeneity Measurements

In order to evaluate the deviation of $B_{1,2}$ and $B_z$ inside a certain volume, it is necessary to enumerate different sources of uncertainty in the measurement of the magnetic field value. These sources can be corrected in the measurement chain depicted in Figs. 6 and 7 by enhancing the performance of the FGM. Also, note that these sources are not related with the design of $\mathrm{Tr}_{1,2}$ or the double Helmholtz coil but with the practical implementation of the FGM. Table II shows the different sources of uncertainty of the magnetic field identified during the design and measurement processes. The sources are divided in phenomena affecting $B_{1,2}$ and phenomena affecting $B_z$.

Some uncertainties affecting the measurement of $B_{1,2}$ and noise produced in the excitation currents were identified during the design process of the measurement chain depicted in Fig. 7. Three different sources of uncertainty were identified. The pick-up coils placed in the measurement head (see Fig. 7) slightly changed their angular orientation during the movement along the $z$-axis and they did not present the same angular orientation with respect to the $x$- and $y$-axes for every point. Therefore, considering the theoretical surface of the pick-up coils, $\mathrm{S}_{\mathrm{theo}}$, as the surface perpendicular to the direction of $B_{1,2}$ ($2 \times 2$ mm$^2$), an uncertainty modeled as an effective surface, $\mathrm{S}_{\mathrm{eff}}$, was introduced. The voltage induced in each coil by $B_{1,2}$ is consequently given by (2), and the effective surface of the coil is given by (3). Therefore, the uncertainty of the magnetic field is given by (4)

$$V_{\mathrm{pcoil}}^{1,2} = B_{1,2} S_{\mathrm{eff}} \omega \tag{2}$$

$$S_{\mathrm{eff}} = S_{\mathrm{theo}} \cos\theta_\Delta \tag{3}$$

$$\Delta B = \pm \| 1 - \cos\theta_\Delta \| \tag{4}$$

where $\theta_\Delta$ is the deviation of the normal vector to the surface $\mathrm{S}_{\mathrm{theo}}$ with respect to the vector defined by the magnetic flux density to be measured ($B_{1,2}$). Considering an estimated $\theta_\Delta = \pm 1.5°$, the deviation from the value of the magnetic flux density is $\sim \pm 0.13\%$.

Before the voltage induced in the pick-up coils by $B_{1,2}$ is recorded by the oscilloscope, the signal is amplified by the instrumentation amplifiers. The voltage gain, $\mathrm{G}_v$ is defined in the following equation. Considering tolerances of $\Delta R_{\mathrm{G}} = \pm 1\%$ for the resistor $\mathrm{R}_{\mathrm{G}}$, the final uncertainty at the first order is $\sim \pm 0.1\%$:

$$\mathrm{G}_v = 1 + \frac{50\ \mathrm{k\Omega}}{R_{\mathrm{G}}} \rightarrow \Delta \mathrm{G}_v = \frac{50\ \mathrm{k\Omega}}{R_{\mathrm{G}}} \Delta R_{\mathrm{G}}. \tag{5}$$

Despite the temperature drift of the magnetic flux densities was corrected by measuring the current through the DHD coils, this measurement was performed with an oscilloscope able to provide up to $\pm$1-mV accuracy. This accuracy results in sharp steps in the measurements of $B_{1,2}$ of $\sim \pm 5.3\ \mu$T. Considering the values of $B_{1,2}$ measured at the center of $\mathrm{Tr}_{1,2}$, the steps result in an uncertainty of $\pm 0.35\%$. Finally, the theory of error propagation provides the total contribution to these sources. In the worst case scenario, the final uncertainty is $\sim \pm 0.6\%$.

The same uncertainty analysis can be applied to the measurement of $B_z$. Both sensors (at the center of the mobile platform and 15 mm away from the center) measure the magnetic flux density perpendicular to their surface. Therefore, uncertainties observed in measurements respond to (4) as described for the pick-up coils. However, in this case, the angles considered are constrained to $\pm 0.5°$ due to the stability of the positioning platform where the sensors are placed (see Fig. 6). For both sensors, the uncertainty is $\sim \pm 0.004\%$.

Also, both sensors are configured with resistors of 1% tolerance. Therefore, if the uncertainty in the sensor voltage gain, $G_v$, is given by the following equation, where $R_2$ and $R_3$ are the resistances configuring the voltage gain of the sensor, the relative uncertainty for both sensors are $\sim\pm 0.16\%$ and $\sim\pm 0.4\%$, respectively

$$\Delta G_v = 2\frac{R_3}{R_2}0.004\frac{\text{mV}}{\text{mT}}. \tag{6}$$

These sources of uncertainty are related to the measurement chain of the $B_z$. However, as it was explained earlier for the measurement of $B_{1,2}$, the KIKUSUI power supply has a limit for the accuracy of the output current which results in an uncertainty in $B_z$. In this case, the error in the output current is $\sim\pm 5$ mA which corresponds to a field uncertainty of 0.5% for both sensors. At the end, the measurements of $B_z$ are affected by total deviations of $\sim\pm 0.6\%$ at the $z$-axis and $\sim\pm 0.8\%$ 15 mm away from it.

In summary, the presented sources of inhomogeneities affect the measurements of the magnetic flux density obtained with the FGM. Therefore, the uncertainty observed in the measurement of the magnetic flux density can be reduced by considering the obtained values.

## IV. Characterization of the MAFS RF Magnet

In order to characterize the magnetic field created by the assembly described in Section II, the magnetic flux densities generated by $Tr_{1,2}$ and the $Z$-coil were measured separately. However, in both cases, the measurement procedure was the same.

### A. Characterization of the RF Fields, $B_{1,2}$

For the RF fields, we placed the FGM (see Section III) with the pick-up coils at the end of the mobile platform. We moved along the $z$-axis the mobile platform taken measurements from the central sensors every 5 mm. Then, we repeated the movement for the sensors placed 15 mm away in six different angular positions. In every measurement, the current through the coil was monitored with a commercial current probe (N278A from AGILENT TECH.).

The homogeneity was evaluated by comparing the measurements from the sensors placed 15 mm away from the center of the measurement tip with the measurements performed with the centered sensor. This comparison was performed along the different $z$-axes according to the following equation:

$$\Delta = \frac{|B(0) - B_\theta|}{B(0)} \tag{7}$$

where $B(0)$ is the magnetic flux density at the center of $Tr_{1,2}$ and $B_\theta$ corresponds to the different measurements taken along the $z$-axes (including the central axis).

Fig. 9(a) shows the values of $B_{1,2}$ at the centered $z$-axis of $Tr_{1,2}$. They are compared with numerical simulations of the ideal winding of $Tr_{1,2}$ (integrations of the Biot–Savart law). Considering a maximum deviation of $\pm 2°$ for $\alpha$ (see Section II) in both windings, the measurements fit well with the simulations. At the center of $Tr_{1,2}$, these resonators produce $B_1 \sim 1.6$ and $B_2 \sim 1.35$ mT/$A_{rms}$.

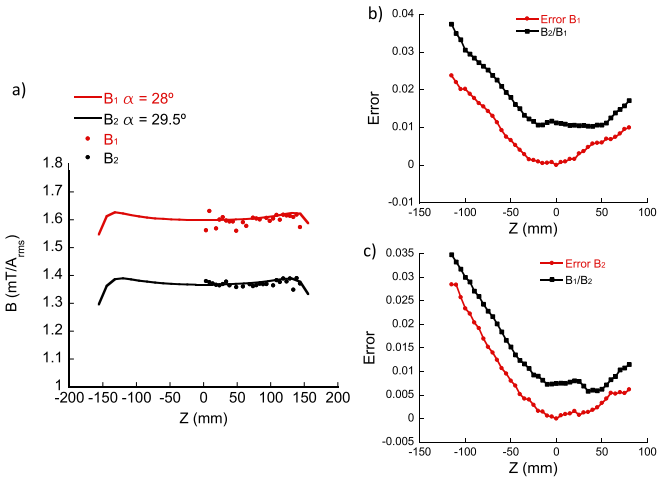


Fig. 9. Measurements of the magnetic flux density produced for $Tr_{1,2}$. $B_{1,2}$ measurements were taken every 5 mm and 16 scans of the RF signal were acquired along the central $z$-axis and along 6 axes placed at 6 different angular orientations (every 60°). (a) Measurements of $B_{1,2}$ inside $Tr_{1,2}$ compared with numerical integration of the Biot–Savart law when certain deviation of $\alpha$ (tilting angle of the windings) is allowed in both windings. (b) Relative error of $B_1$ (●) along the central $z$-axis and $B_2/B_1$ ratio (■). (c) Relative error of $B_2$ (●) along the central $z$-axis and $B_1/B_2$ ratio (■).

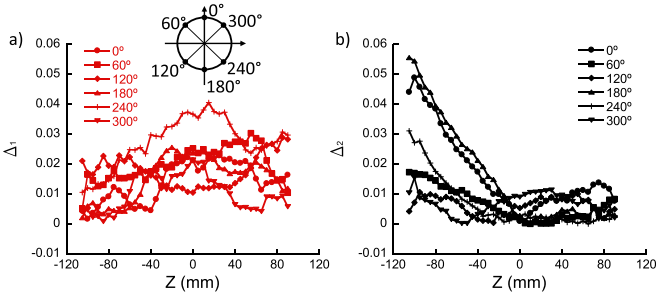


Fig. 10. Deviation of magnetic flux density measured at 15 mm away from the center, with respect to $B_{1,2}$ measured at the center of $Tr_{1,2}$. $B_\theta$ measurements were taken every 5 mm and 16 scans of the RF signal were acquired at six different angular orientations (every 60°). a) Deviations of $B_1$ along the six different orientations. b) Deviations of $B_2$ along the six different orientations.

Fig. 10 shows the deviation of the magnetic flux density measured along the axes placed at the six different angular positions with respect to the value of the magnetic flux density measured at the center of $Tr_{1,2}$ [see Fig. 9(a)]. They were calculated according to (7), where $B_\theta$ corresponds to the measurements from the pick-up coils at 15 mm.

The deviation from the central value, $B(0)$, of $B_2$, $\Delta_2$, is $\sim 1\%$ or less at every angular orientation [see Fig. 10(b)]. This value is in good agreement with the design expectations. However, the deviation of $B_1$, $\Delta_1$, is $\leq 4\%$ at every angular orientation, which is almost four times the expected value from the design specifications. This increment in the deviation is caused by the manual alignment of the layers of $Tr_1$. The misalignment produces an increase in the orthogonal component ($B_2$ for Tr1) outside the center and the desired component reduces its amplitude [24]. This matches perfectly with the results shown in Fig. 9(b) and (c) where a higher orthogonal component is observed for $B_2$ measured at the center of $Tr_1$.

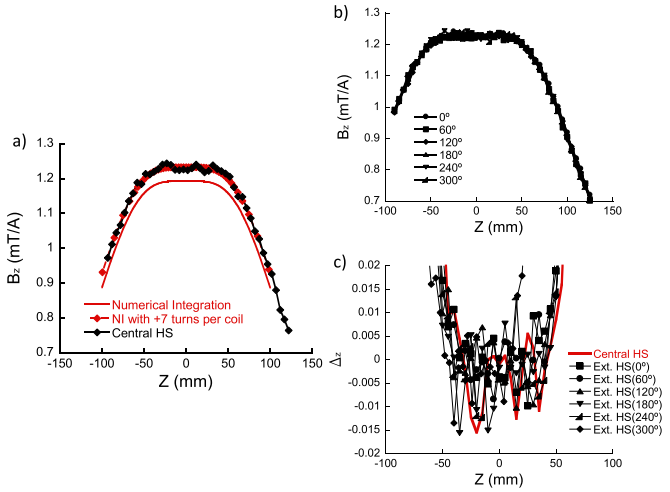


Fig. 11. Measurements of the magnetic flux density produced by $Z$-coil. Measurements were taken every 5 mm and 16 scans of the voltage read from the multimeter were taken. (a) Measurements of $B_z$ inside $Z$-Coil compared with simulations performed with COMSOL. (b) Magnetic flux density measured at the six angular positions 15 mm away from the center of the $Z$-coil. The error of the AD22151 Hall sensor with the gain selected at this position makes difficult to analyze the homogeneity with resolutions $\leq$1% (c) Relative error of $B_z$ (—) along the central $z$-axis and relative error of $B_z$ measured with the Hall sensor placed 15 mm from the center of the measurement tip along the $z$-axis and placed at the six angular positions cited in Fig. 10.

These results must be evaluated considering the uncertainties presented in Section III-C. The magnetic field uncertainties in the measurement of $B_{1,2}$ are $\sim\pm$0.57% for both fields. Therefore, there is a reduction of the homogeneity limit inside the cylindrical volume to be considered. This reduction is expected to be confirmed during the NMR experiments devoted to fine tune the RF magnet fields.

### *B. Characterization of the dc Field, $B_z$*

Fig. 11 shows the measurements performed with the Hall sensors. Fig. 11(a) demonstrates the agreement between measurements and simulations performed during the design of $Z$-coil. The magnetic flux density produced by the double Helmholtz pair is $\sim$1.225 mT/A. This measurement is higher than the value predicted with simulations ($\sim$1.19 mT/A). However, when two extra turns are distributed in every winding of the $Z$-coil, the measurements match perfectly with the simulations. These extra turns have to be considered due to imperfections during the manual winding of the coils. The distribution of these extra turns degrades the homogeneity inside the cylindrical volume under study (30 $\times$ 30 mm). Fig. 11(b) shows the measurements along the six longitudinal axes placed according to Fig. 10. We observe that within the noise, there is not angular deviation of the field observed and we only expect a radial variation of the intensity of $B_z$.

Fig. 11(c) shows the error along axes placed 15 mm away the center axis (at the six angular positions) and the center axis itself, according with (7). The deviations, $\Delta_z$, are all around 0.5% of $B_z(0)$. These deviations are due to the distribution of extra turns commented earlier. Differences in the number of turns distributed in each coil of the two Helmholtz pairs produce asymmetric magnetic flux densities that added-up increase $\Delta_z$. However, the main value of these deviations shows that $B_z$ presents a radial distribution, changing its intensity in any angular orientation in the same way. Therefore, $\Delta_z$ decrease when $B_z$ is observed at radii $\leq$15 mm. Luckily, this radial distribution of $\Delta_z$ can be easily compensated with an extra coil placed at the center of the $Z$-coil [25]. The noise observed in the deviations fits perfectly with the results presented in Section III-C where uncertainties of $\sim\pm$0.6% and $\sim\pm$0.8% were obtained after error analysis of the measurement chain.

Therefore, the $Z$-coil is able to produce $\sim$10 mT when the current source (see Section II) delivers $\sim$8 A, which results in 112-W dissipated in the $Z$-coil. The volume where the field deviates less than 0.5% is defined by a cylinder of $30 \times 30$ mm in length and diameter. A passive shimming strategy, like an extra coil placed at the center of the $Z$-coil is needed in order to enhance the homogeneity and reduce the 0.5% limit.

## V. Conclusion

An MAFS magnet based on RF signals has been successfully built and characterized. The assembly consists of two transverse resonators (DHD coils) and a double Helmholtz pair producing a combination of ac and dc magnetic fields. The electromagnets form a compact device of $\sim$1.1 m height and 15 kg weight enclosed in a grounded aluminum frame. In order to generate the magnetic fields, a double output signal generator, a pair of current amplifiers delivering 300 W up to 12 kHz, and a dc current source were used.

The magnet was characterized by measuring the magnetic flux density of the different electromagnets that conform the assembly. These measurements were carried out with a homemade FGM able to measure magnetic flux densities of ac and dc magnetic fields in the $xy$ plane and $z$-axis every 5 mm. The accuracy of the system was achieved through a calibration process and its resolution in every measurement is $\leq\pm 26$ $\mu$T for the RF fields and $\leq$70 $\mu$T for the dc field, as it was demonstrated in Section III-A.

The RF magnetic flux densities produced by $\mathrm{Tr}_{1,2}$ were characterized along the central $z$-axis. Values of 1.6 and 1.35 $\mathrm{mT/A_{rms}}$ were obtained on a range of 30 mm around the center of the coils. These values change less than 4% and 1%, respectively, inside a cylindrical volume of 30 $\times$ 30 mm. The deviations can be corrected by micropositioning of the layers forming $\mathrm{Tr}_{1,2}$. Deviations from expected homogeneity are due to misalignments of the layers forming $\mathrm{Tr}_{1,2}$. At the same time, the orthogonal component produced by each resonator can be compensated with the RF signals (amplitude and phase) from the signal generator.

The dc magnetic flux density produced by the $Z$-coil is 1.225 mT/A. The measurements along the axes placed 15 mm away from the center show that this value changes $\leq$0.5% inside a cylindrical volume of 30 $\times$ 30 mm. Deviations from simulations come from the manual winding of each coil forming the $Z$-coil. At the end, dc current source feeding this coil ensures a $B_z$ field of 10 mT in that volume.

Therefore, our MAFS RF prototype is able to produce magnetic flux densities of 10 mT with precessing

frequencies of 1–12 kHz and a precessing angle, controlled by the amplitude of $B_{ROT}$, adjustable to the magic angle (54.74°). With improvements in the homogeneity of $B_1$ by mechanically alignment of the layers forming $Tr_1$ and passive shimming of the $Z$-coil, we consider the presented prototype as a proof of concept of the technology needed to produce an RF-MAFS magnetic field. This prototype can be properly debugged and complemented with the necessary hardware in order to perform NMR and MRI experiments in the future.

## ACKNOWLEDGMENT

The authors would like to thank J. M. Gomez-Perez for his invaluable help with EM simulations and L. Mori-Carrascal for her insights into experimental issues.

## REFERENCES

[1] W. I. Goldburg and M. Lee, "Nuclear magnetic resonance line narrowing by a rotating RF field," *Phys. Rev. Lett.*, vol. 11, pp. 255–258, Sep. 1963.
[2] C. A. Meriles, D. Sakellariou, A. Moulé, M. Goldman, T. F. Budinger, and A. Pines, "High-resolution NMR of static samples by rotation of the magnetic field," *J. Magn. Reson.*, vol. 169, no. 1, pp. 13–18, Jul. 2005.
[3] D. Sakellariou, C. A. Meriles, R. W. Martin, and A. Pines, "NMR in rotating magnetic fields: Magic-angle field spinning," *Magn. Reson. Imag.*, vol. 23, no. 2, pp. 295–299, Feb. 2005.
[4] A. Abragam, *The Principles of Nuclear Magnetism* (International Series of Monographs on Physics). Oxford, U.K.: Oxford Univ. Press, 1983.
[5] M. J. Duer, Ed., *Introduction to Solid-State NMR Spectroscopy*. Hoboken, NJ, USA: Wiley, 2005.
[6] M. H. Levitt, *Spin Dynamics: Basics of Nuclear Magnetic Resonance*. Hoboken, NJ, USA: Wiley, 2008.
[7] E. R. Andrew, A. Bradbury, and R. G. Eades, "Nuclear magnetic resonance spectra from a crystal rotated at high speed," *Nature*, vol. 182, no. 4650, p. 1659, Dec. 1958.
[8] E. R. Andrew and R. G. Eades, "Possibilities for high-resolution nuclear magnetic resonance spectra of crystals," *Discuss. Faraday Soc.*, vol. 34, pp. 38–42, Jan. 1962.
[9] O. Natt and J. Frahm, "*In vivo* magnetic resonance imaging: Insights into structure and function of the central nervous system," *Meas. Sci. Technol.*, vol. 16, no. 4, pp. 235–249, Jul. 2005.
[10] R. M. Henkelman, G. J. Stanisz, J. K. Kim, and M. J. Bronskill, "Anisotropy of NMR properties of tissues," *Magn. Reson. Med.*, vol. 32, no. 5, pp. 592–601, Jan. 1994.
[11] E. M. Haacke, *Magnetic Resonance Imaging: Physical Principles and Sequence Design*. Hoboken, NJ, USA: Wiley, 1999.
[12] J. Voccio *et al.*, "Magic-angle-spinning NMR magnet development: Field analysis and prototypes," *IEEE Trans. Appl. Supercond.*, vol. 23, no. 3, Jun. 2013, Art. no. 4300804.
[13] J. Voccio *et al.*, "A 1.5-T magic-angle spinning NMR magnet: 4.2-K performance and field mapping test results," *IEEE Trans. Appl. Supercond.*, vol. 25, no. 3, pp. 1–5, Jun. 2015.
[14] D. Sakellariou, C. Hugon, A. Guiga, G. Aubert, S. Cazaux, and P. Hardy, "Permanent magnet assembly producing a strong tilted homogeneous magnetic field: Towards magic angle field spinning NMR and MRI," *Magn. Reson. Chem.*, vol. 48, no. 12, pp. 903–908, Dec. 2010.
[15] J. V. M. McGinley, M. Ristic, and I. R. Young, "A permanent MRI magnet for magic angle imaging having its field parallel to the poles," *J. Magn. Reson.*, vol. 271, pp. 60–67, Oct. 2016.
[16] B. Blümich, F. Casanova, and A. Appelt, "NMR at low magnetic fields," *Chem. Phys. Lett.*, vol. 477, nos. 4–6, pp. 231–240, Aug. 2009.
[17] E. Fukushima and J. A. Jackson, "Unilateral magnet having a remote uniform field region for nuclear magnetic resonance," U.S. Patent 6 489 872 B1, Dec. 3, 2002.
[18] W.-H. Chang, J.-H. Chen, and L.-P. Hwang, "Single-sided mobile NMR with a Halbach magnet," *Magn. Reson. Imag.*, vol. 24, no. 8, pp. 1095–1102, Oct. 2006.
[19] W.-H. Chang, J.-H. Chen, and L.-P. Hwang, "Single-sided mobile NMR apparatus using the transverse flux of a single permanent magnet," *Magn. Reson. Imag.*, vol. 28, no. 1, pp. 129–138, Jan. 2010.
[20] B. Manz *et al.*, "A mobile one-sided NMR sensor with a homogeneous magnetic field: The NMR-MOLE," *J. Magn. Reson.*, vol. 183, no. 1, pp. 25–31, Nov. 2006.
[21] P. Andris and I. Frollo, "Optimized measurement of magnetic field maps using nuclear magnetic resonance (NMR)," *Meas. Sci. Technol.*, vol. 22, no. 4, pp. 1–5, Oct. 2011.
[22] S. R. Trout, "Use of Helmholtz coils for magnetic measurements," *IEEE Trans. Magn.*, vol. 24, no. 4, pp. 2108–2111, Jul. 1988.
[23] J. Mispelter, M. Lupu, and A. Briguet, *NMR Probeheads for Biophysical and Biomedical Experiments: Theoretical Principles and Practical Guidelines*. London, U.K.: Imperial College Press, 1963.
[24] C. L. Goodzeit, M. J. Ball, and R. B. Meinke, "The double-helix dipole—A novel approach to accelerator magnet design," *IEEE Trans. Appl. Supercond.*, vol. 13, no. 2, pp. 1365–1368, Jun. 2003.
[25] M. Piotto, K. Elbayed, J.-M. Wieruszeski, and G. Lippens, "Practical aspects of shimming a high resolution magic angle spinning probe," *J. Magn. Reson.*, vol. 173, no. 1, pp. 84–89, Mar. 2005.

**Javier Alonso-Valdesueiro** was born in Madrid, Spain, in 1980. He received the Degree in telecommunication engineering from the University of Alcala, Madrid, in 2006, and the Ph.D. degree from the Polytechnic University of Catalonia, Barcelona, Spain, in 2011.

From 2012 to 2017, he was with C.E.A Center, France and then with the University of Southampton, where he was involved in electronic instrumentation for NMR experiments. He is currently a Marie Sklodowska-Curie Fellow with the University of the Basque Country, Leioa, Spain. His current research interests include MRI RF novel hardware and methodologies, electronic instrumentation, and new NMR perspectives.

**Beatriz Sisniega** was born in Navarra, Spain, in 1994. She received the Degree in physics from the University of the Basque Country, Leioa, Spain, in 2017, and the M.Sc. degree in science of new materials from the University of Cantabria, Santander, Spain, in 2018.

She is currently involved in the development of new hardware and methodology for nuclear magnetic resonance and magnetic resonance imaging.

**Irati Rodrigo** was born in Bilbao, Spain, in 1989. She received the Degree in physics and electronics engineering from the University of the Basque Country, Leioa, Spain, in 2013, and the joint M.Sc. degree in biomedical engineering from UPV/EHU, Leioa, and the National University of Asuncin, Paraguay, in 2015. She is currently pursuing the Ph.D. degree at the University of the Basque Country, with a focus on the design and development of novel experimental techniques for magnetic hyperthermia.

**Jorge Pérez-Muñoz** was born in Fuenmayor, Spain, in 1991. He received the Degree in physics from the University of Cantabria, Santander, Spain, in 2015, and the M.Sc. degree in science of new materials from University of the Basque Country, Leioa, Spain, in 2016, where he is currently pursuing the Ph.D. degree, with a focus on the development of new magnetic hyperthermia systems applied in cancer treatments.

**Juan-Mari Collantes** received the Ph.D. degree in electronics from the University of Limoges, Limoges, France, in 1996.

Since 1996, he has been an Associate Professor with the Electricity and Electronics Department, University of the Basque Country, Leioa, Spain. From 1996 to 1998, he was an Invited Researcher with Agilent Technologies (formerly the Hewlett-Packard Company), Santa Rosa, CA, USA. In 2003, he was with French Space Agency, Toulouse, France, where he was involved in power amplifier analysis, simulation, and modeling. His current research interests include nonlinear analysis and design of microwave circuits, microwave measurement techniques, and noise characterization.

**Fernando Plazaola** was born in Gipuzkoa, Spain, in 1958. He received the Degree in physics from the Complutense University of Madrid, Madrid, Spain, in 1982, and the Ph.D. degree in physics from the University of the Basque Country (UPV/EHU), Leioa, Spain, in 1986, with a focus on materials science.

From 1982 to 1985, he held a Pre-Doctoral position with the Laboratory of Physics, Helsinki University of Technology (HUT), Espoo, Finland. In 1997, he was a Guest Scientist with HUT. Since 1998, he has been a Full Professor of applied physics with UPV/EHU. Since 1999, he has been the Head of the Laboratory of Nuclear Techniques applied to Material Science, Science and Technology Faculty, UPV/EHU. Since 2003, he has been a Visiting Professor with HUT. His current research interests include magnetic materials and defect studies in compound semiconductors and polymers.